Fourier Transform approach to homogenization of frequency dependent heat transfer in porous media

Quy-Dong To, Guy Bonnet

Fourier Transform approach to homogenization of frequency dependent heat transfer in porous media

Quy-Dong To[a,*], Guy Bonnet[a]

[a]*Laboratoire MSME, Univ Gustave Eiffel, CNRS UMR 8208,F-77454 Marne-la-Vallée, France*

Abstract

The Fourier Transform method is used to solve frequency dependent heat transfer problems. The periodic Lippmann-Schwinger (LS) integral equation in Fourier space with source term is first formulated using discrete Green operators and modified wavevectors which can then be solved by iteration schemes. The objective is to solve the local problem involving strong contrast heterogeneous conductive material, with application to gas-filled porous media with both perfect and imperfect Kapitza boundary conditions at the bi-material interface. The effective parameters such as the dynamic conductivity and the thermal permeability in the acoustics of porous media are also derived from the cell solution. Numerical examples show that the schemes converge fast and yield accurate results when compared with analytical solution for benchmark problems. The formulation of the method is built using static or dynamic Green operators and can be applied to pixelized microstructure issued from tomography images.

Keywords: Fourier Transform method, Strong contrast homogenization, Heat transfer, Dynamic thermal permeability, Porous media

*Corresponding author. Email: quy-dong.to@univ-eiffel.fr

1. Introduction

Determining the overall behavior of heterogeneous media is the main focus of homogenization theory (Milton, 2002; Torquato, 2001; Nemat-Nasser and Hori, 2013). Based on the local boundary value problem on a Representative Volume Element (RVE), average quantities can be obtained to establish the macroscoscopic relations for the equivalent homogenized material. By construction, the distribution of the heterogeneous materials in the RVE can be either random or periodic.

The homogenization of periodic materials can be addressed by double scale asymptotic procedures (Bensoussan et al., 1978). By developing the local problem with respect to the scale separation ratio ε, a large number of macroscopic models can be derived, whose form can be different from the local constitutive behavior. Considering the heat transfer problem under harmonic excitation at a given frequency ω, Auriault (1983) showed that for large contrasts of thermal conductivity, the constitutive equation is frequency dependent, resulting in a memory kernel for the transient behavior. It is worthwhile noticing that the local cell problem is of the same type as the one related to "dynamic thermal permeability" that appears in the computation of the dynamic compressibility of a gas within a porous medium (Lafarge et al., 1997).

The main objective of the present work is to address the frequency dependent heat transfer problem in a periodic cell. With the increasing capabilities of computing power, solving problems on realistic microstructures becomes more accessible. Numerical methods are developed to handle both tomographic or computer generated images. Compared with other methods such as Finite Element Method or Random Walk, methods based on Fourier Transform benefit from serious advantages. The methods rely directly on pixelization of the simulation domain and the robustness of the Fast Fourier

Transform algorithm when dealing with periodicity. Additionally, the resolution based on iterative schemes is fast and yields accurate overall properties.

Although the Lippmann-Schwinger (LS) integral equations had been derived previously (Brown Jr, 1955; Kröner, 1977) for micromechanics problems, Moulinec and Suquet (1994); Michel et al. (1999) proposed to use iterative schemes combined with Fast Fourier Transform to solve numerically these equations. A broad range of engineering problems such as fluid flows (Nguyen et al., 2013; Bignonnet, 2020), non linear behavior (Michel et al., 2001), finite strain (De Geus et al., 2017), Kapitza interface problem in composites (Monchiet, 2018) etc.... have been treated by the method since then. Efforts have been made to accelerate the convergence at high contrast ratio such as the polarization schemes (Eyre and Milton, 1999; Monchiet and Bonnet, 2013), variational schemes (Brisard and Dormieux, 2010), Newton-Krylov solvers (Brisard and Dormieux, 2012; Vondřejc et al., 2014; Zeman et al., 2010; Schneider, 2019).

For porous materials where the contrast ratio becomes infinite, the convergence becomes the main issue. It is shown that most of iterative schemes fail to satisfy the divergence free and rotational free criteria (Moulinec and Silva, 2014). To overcome those limitations, To and Bonnet (2020); To et al. (2021) recently proposed a class of iteration scheme based on boundary integral equation. Another interesting technique is to use discrete Green tensors and modified wavevectors as derived from finite difference approximation (Willot et al., 2014). In a comparison between different iterative schemes, (Moulinec et al., 2018) the authors stated "continuous Green's operator performs better for moderate contrast whereas discrete operators should be used for large contrast". Since the latter is suitable for pixelized microstructure, it will be adopted to solve the heat transfer problem.

The paper is organized as follows. First, the important results of asymptotic homogenization theory in the case of large contrasts between the properties of constituents is recalled. Next, the LS integral equation for the heat transfer problem with a source term using modified Green tensors is presented. Combined with the immersed interface technique (Peskin, 1972), the iterative schemes are then derived for a large class of boundary value problems: prescribed flux, prescribed temperature, temperature jump, temperature dependent source term. These schemes are then used to solve the frequency dependent heat transfer problem and results are compared with analytical solutions from the literature.

2. Heat transfer problems from asymptotic homogenization theory

2.1. Strong contrast composites and effective frequency dependent heat capacity

According to the asymptotic homogenization theory, the macroscopic law is constructed based on the length scale ratio

$$\varepsilon = \frac{l_{micro}}{L_{macro}} \ll 1 \tag{1}$$

where l_{micro} and L_{macro} are the characteristic length at the micro and macro scales of the heterogeneous material. In addition, all physical quantities are treated as functions of two space variables, the macroscopic space variable $\boldsymbol{X}$ and the microscopic space variable $\boldsymbol{x}$, with $\boldsymbol{x} = \boldsymbol{X}/\varepsilon$ representing local fluctuations within the microstructure.

Let us consider a porous material whose solid skeleton is characterized by conductivity κ_s and thermal capacity c_s filled by a fluid characterized by κ_g and c_g as in Fig. 1. When $\kappa_g/\kappa_s = \mathcal{O}(1)$ and $\rho_s c_s/(\rho_g c_g) = \mathcal{O}(1)$ the asymptotic expansion method (Auriault, 1983) shows that the porous material behaves as a material with the effective conductivity given by the usual

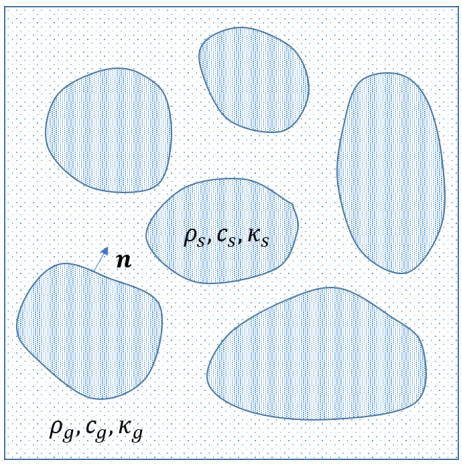

Figure 1: Sketch of two phase material with high contrast conductivity ratio $\kappa_g/\kappa_s \ll 1$.

homogenization method, i.e the static case. In this case, the effective thermal capacity is equal to the volume average of local thermal capacities.

When the thermal conductivity of the gas is very small compared to the one of the solid, this result is no longer valid. It is shown that if $\kappa_g/\kappa_s = \mathcal{O}(\varepsilon^2)$ and $\rho_s c_s/(\rho_g c_g) = \mathcal{O}(1)$, the porous medium is characterized by a frequency dependent thermal capacity that is obtained from a dynamic localization problem which writes:

$$\kappa_g \Delta_{\boldsymbol{x}} \theta - i\omega \rho_g c_g \theta - i\omega \rho_g c_g T = 0, \tag{2}$$

and

$$\theta = 0 \quad \text{at the solid/gas boundary} \tag{3}$$

where $T(\boldsymbol{X})$ is the amplitude of the macroscopic temperature, that depends only on the macroscopic space variable $\boldsymbol{X}$. The solution of this equation

leads to a local value of θ linearly related to T:

$$\theta(\boldsymbol{X}, \boldsymbol{x}, \omega) = -\chi(\boldsymbol{x}, \omega) T(\boldsymbol{X}) \tag{4}$$

The macroscopic balance of energy can be written:

$$\mathrm{div}_{\boldsymbol{X}}(\kappa_{eff} \nabla_{\boldsymbol{X}} T) = (\rho c)_{eff} i\omega T \tag{5}$$

where κ_{eff} is the effective conductivity and $(\rho c)_{eff}$ is the effective dynamic thermal capacity given by

$$(\rho c)_{eff} = \langle \rho c \rangle - \frac{\rho_g c_g}{|V|} \int_{V_g} \chi(\boldsymbol{x}, \omega) d\boldsymbol{x}. \tag{6}$$

Here, V is the volume of the periodic cell, V_g is the volume of fluid within the cell and $\langle\rangle$ denotes the volume average over the cell.

2.2. Heat transfer due to acoustic wave in fluid filled porous media

In this case, the dynamic behavior is governed at the local scale by mass conservation, Navier-Stokes equation, heat equation and the equation of state for the gas. The scaling of these equations with suitable renormalization of the physical coefficients has been described in Auriault et al. (2010) and Boutin et al. (1998). The asymptotic method leads to the following results:

- At highest order in ε, the macroscopic pressure P depends only on the macroscopic space variable.
- At the following order, the local temperature within the gas is the solution of

$$\kappa_g \Delta_{\boldsymbol{x}} \theta - i\omega \rho_g c_g \theta + i\omega P = 0, \tag{7}$$

with $\theta = 0$ on the boundary of the fluid domain. It is noteworthy that equation (7) has the same form as (2) where the driving force $i\omega P$ plays

the same role as $-i\omega\rho_g c_g T$

The solution is proportional to $i\omega P$ and it is natural to introduce a variable $\overline{\theta}$ given by $\overline{\theta} = \frac{\theta\kappa_g}{i\omega P}$ that is solution of:

$$\Delta\overline{\theta} - \frac{\overline{\theta}}{\delta^2} + 1 = 0, \tag{8}$$

where δ is the complex length

$$\delta = \sqrt{\frac{\kappa_g}{i\omega\rho_g c_g}}. \tag{9}$$

The volume average of $\overline{\theta}$ over the fluid volume is given by:

$$\overline{\Theta} = \frac{1}{|V_g|}\int_{V_g} \overline{\theta} d\boldsymbol{x} \tag{10}$$

with $\overline{\Theta}$ being a macroscopic physical parameter called the "thermal permeability" (Lafarge et al., 1997). For a given microstructure, $\overline{\Theta}$ only depends on the complex length δ, which is a function of frequency by (9), or $\overline{\Theta} = \overline{\Theta}(\delta(\omega))$. This parameter plays an important role in the determination of the effective dynamic compressibility.

From equations (2) and (7), it can be seen that these equations are the same when replacing P by $-\rho_g c_g T$. It follows that χ in (4) is related to θ^* by

$$\chi = \frac{\overline{\theta}}{\delta^2}. \tag{11}$$

Finally, the effective dynamic capacity is obtained from the thermal permeability by:

$$(\rho c)_{eff} = \langle\rho c\rangle - \frac{1}{\delta^2}\frac{\rho_g c_g}{|V|}|V_g|\,\overline{\Theta} = \langle\rho c\rangle - \frac{1}{\delta^2}\nu_g\rho_g c_g\overline{\Theta} \tag{12}$$

where ν_g is the volume concentration of gas.

In the following, the problem of dynamic thermal permeability will be solved, knowing that the dynamic thermal capacity can be obtained from this relation.

2.3. Temperature jump boundary conditions

In addition to the perfect boundary conditions (3), we also study the case where there is a temperature jump, also called temperature slip, in the form (Kapitza, 1941):

$$\theta(\boldsymbol{x}) = l\nabla\theta(\boldsymbol{x})\boldsymbol{n}(\boldsymbol{x}) = \frac{\kappa_g}{\kappa_{int}}\nabla\theta(\boldsymbol{x})\boldsymbol{n}(\boldsymbol{x}) \quad \text{at solid/gas boundary} \tag{13}$$

with $\boldsymbol{n}$ being the normal vector, l the slip length, κ_{int} the interface coefficient. The phenomenon is frequently encountered at gas flows characterized by high Knudsen number, i.e when the mean free path is comparable to the characteristic size of the pore (Umnova et al., 2009; Chastanet et al., 2004). Microscopically, it can be quantified by the collision between the gas atoms and the solid wall (Liao et al., 2018a,b). For perfect interface, $l = 0$ and $\kappa_{int} = \infty$, the perfect boundary conditions (3) is recovered.

It is noteworthy that the slip condition can be recovered as the limit case of a layer of large conductivity and small thickness at the interface between the phases, when the thickness tends to zero. This does not affect the distribution of heat capacity and it will be considered that the result of homogenization theory (Auriault et al., 2010) is also valid in this case, the difference being only to account for the temperature jump in the localization problem.

3. Fourier Transform resolution method using the static Green tensor

For simple geometries (plane slits, cylindrical interfaces), the boundary value problem (8-9) can be solved in a closed form, but in the general case a suitable numerical solution becomes necessary. In this section, a numerical solution based on a FFT formulation is presented.

3.1. Periodic heat equation with source term and associated discrete operators

Let us consider a heterogeneous material where the local conductivity $\kappa(\boldsymbol{x})$ is a periodic function of the coordinate $\boldsymbol{x}$ with period V of dimensions $V = L_1 \times L_2 \times L_3$ in the Cartesian coordinate system. The governing equations of the problem are the following

$$\boldsymbol{e} = \boldsymbol{E} - \nabla\theta, \quad \operatorname{div}(\boldsymbol{j}) + s = 0, \quad \boldsymbol{j} = \kappa\boldsymbol{e} \tag{14}$$

where θ, $\boldsymbol{e}$, $\boldsymbol{j}$ and s are the V periodic temperature, (minus) temperature gradient, heat flux and source term with volume averages Θ, $\boldsymbol{E}$, $\boldsymbol{J}$ and 0, i.e

$$\langle\theta(\boldsymbol{x})\rangle = \Theta, \quad \langle\boldsymbol{e}(\boldsymbol{x})\rangle = \boldsymbol{E}, \quad \langle\boldsymbol{j}(\boldsymbol{x})\rangle = \boldsymbol{J}, \quad \langle s(\boldsymbol{x})\rangle = 0. \tag{15}$$

The last condition $\langle s(\boldsymbol{x})\rangle = 0$ is necessary for the compatibility between the periodic flux $\boldsymbol{j}$ and the energy conservation. In general, the source term s can be temperature dependent. Due to the periodicity, the problem can be solved using Fourier series. For a V periodic function $f(\boldsymbol{x})$ of real variable $\boldsymbol{x}(x_1, x_2, x_3)$, it can be written as

$$f(\boldsymbol{x}) = \sum_{\boldsymbol{\xi}} \widehat{f}(\boldsymbol{\xi}) e^{i\boldsymbol{\xi}\boldsymbol{x}}, \quad i = \sqrt{-1} \tag{16}$$

where $\widehat{f}(\boldsymbol{\xi})$ is the Fourier transform of $f(\boldsymbol{x})$, notation $\widehat{f}(\boldsymbol{\xi}) = \mathcal{F}[f(\boldsymbol{x})]$, and function of wave vector $\boldsymbol{\xi}(\xi_1, \xi_2, \xi_3)$

$$\xi_k = 2\pi n_i / L_i, \quad n_i = 0, \pm 1, \pm 2, ..., \pm\infty, \quad i = 1, 2, 3. \tag{17}$$

Numerically, we are limited to finite resolution by bounding n_i with resolution parameter N, i.e $-N \leq n_i \leq N-1$, and solve the problem on collocated grid. It is noted that the resolution parameter N corresponds to resolution $2N$ in real space. For example, if $N = 128$ is adopted for 2D problems, in real space the resolution would be 256×256.

The usual way to produce Green tensor for the FFT method is to use the classical relation between spatial derivative and the product by the wave vector. An alternative is to use a modified Green tensor built as follows using modified wave vectors. As shown in (Willot et al., 2014), the use of modified Green tensors avoids the convergence issues in infinite contrast situations and solution fluctuations due to Fourier series. The spatial derivatives at the grid points $\boldsymbol{x}(n_1 h_1, n_2 h_2, n_3 h_3)$ with $h_i = L_i/2N$ are estimated by forward and backward finite difference. In physical and Fourier space, we have

$$\begin{aligned}
&\text{Forward: } \frac{\partial f}{\partial x_i}(\boldsymbol{x}) = \frac{1}{h_i}\left[f(\boldsymbol{x} + h_i \boldsymbol{e}_i) - f(\boldsymbol{x})\right], \quad \widehat{\frac{\partial f}{\partial x_i}}(\boldsymbol{\xi}) = i k_i \widehat{f}(\boldsymbol{\xi}), \\
&\text{Backward: } \frac{\partial f}{\partial x_i}(\boldsymbol{x}) = \frac{1}{h_i}\left[f(\boldsymbol{x}) - f(\boldsymbol{x} - h_i \boldsymbol{e}_i)\right], \quad \widehat{\frac{\partial f}{\partial x_i}}(\boldsymbol{\xi}) = i k_i^* \widehat{f}(\boldsymbol{\xi}), \\
&i = 1, 2, 3.
\end{aligned} \tag{18}$$

with the modified complex wavevector k_i and its complex conjugate k_i^* being the quantities

$$k_i = \frac{1}{h_i}(e^{i\xi_i h_i} - 1), \quad k_i^* = \frac{1}{h_i}(e^{-i\xi_i h_i} - 1). \tag{19}$$

Next, following Willot et al. (2014), the discrete Green operators $\boldsymbol{P}$, $\boldsymbol{Q}$, $\boldsymbol{H}$ and $\boldsymbol{R}$ are constructed from the modified wavevector $\boldsymbol{k}(k_1, k_2, k_3)$

$$\begin{aligned} \boldsymbol{P}(\boldsymbol{\xi}) &= \frac{\boldsymbol{k} \otimes \boldsymbol{k}^*}{|\boldsymbol{k}|^2}, \quad \boldsymbol{Q}(\boldsymbol{\xi}) = \boldsymbol{I} - \boldsymbol{P}(\boldsymbol{\xi}), \quad \boldsymbol{H}(\boldsymbol{\xi}) = \boldsymbol{I} - 2\boldsymbol{P}(\boldsymbol{\xi}) \\ \boldsymbol{R}(\boldsymbol{\xi}) &= \frac{i\boldsymbol{k}}{|\boldsymbol{k}|^2}, \quad \forall \boldsymbol{\xi} \neq \boldsymbol{0} \end{aligned} \tag{20}$$

and

$$\boldsymbol{P}(\boldsymbol{0}) = \boldsymbol{Q}(\boldsymbol{0}) = \boldsymbol{H}(\boldsymbol{0}) = \boldsymbol{R}(\boldsymbol{0}) = \boldsymbol{0} \tag{21}$$

As a result, the integral equations to solve the heat transfer problem with source term can be obtained (To et al., 2021). Depending on the choice of unknowns, we have, say, for gradient $\boldsymbol{e}$

$$\boldsymbol{e}(\boldsymbol{x}) = \boldsymbol{E} + \frac{1}{\kappa_0}\boldsymbol{R} * s - \boldsymbol{P} * \left[\frac{\kappa - \kappa_0}{\kappa_0}\boldsymbol{e}\right] \tag{22}$$

for the flux $\boldsymbol{j}$

$$\boldsymbol{j}(\boldsymbol{x}) = \boldsymbol{J} + \boldsymbol{R} * s + \boldsymbol{Q} * \left[\frac{\kappa - \kappa_0}{\kappa}\boldsymbol{j}\right] \tag{23}$$

and for the polarization $\boldsymbol{\tau}$

$$\boldsymbol{\tau}(\boldsymbol{x}) = \boldsymbol{T} + 2\boldsymbol{R} * s + \boldsymbol{H} * \left[\frac{\kappa - \kappa_0}{\kappa + \kappa_0}\boldsymbol{\tau}\right], \tag{24}$$

Here the polarization $\boldsymbol{\tau}$ with average $\langle \boldsymbol{\tau}(\boldsymbol{x}) \rangle = \boldsymbol{T}$, is given by

$$\boldsymbol{\tau} = (\kappa + \kappa_0)\boldsymbol{e} = (\kappa + \kappa_0)\boldsymbol{j}/\kappa \tag{25}$$

and $*$ represents convolution operation in the real space. In Fourier space, this operation is equivalent to simple product between the transformed quan-

tities.

The LS equations (22), (23) and (24) can be used to solve the corresponding quantities $\boldsymbol{e}, \boldsymbol{j}, \boldsymbol{\tau}$ by iteration schemes. In addition, the temperature distribution can be recovered from the equivalent relation of (14)

$$\theta(\boldsymbol{x}) = \Theta + \widetilde{\theta}(\boldsymbol{x}), \quad \widetilde{\theta}(\boldsymbol{x}) = -\boldsymbol{R}^* * \boldsymbol{e}. \tag{26}$$

and $\widetilde{\theta}(\boldsymbol{x})$ is the fluctuation $\theta(\boldsymbol{x})$ around the mean value Θ.

3.2. Iteration schemes

Let us start with the LS equations (22), (23) and (24). The common points of those equations are that they have the form

$$\boldsymbol{u}(\boldsymbol{x}) = \boldsymbol{U} + \boldsymbol{A} * s + \boldsymbol{B} * (\epsilon \boldsymbol{u}) \tag{27}$$

where $\boldsymbol{u}$ (which can be either $\boldsymbol{e}$ or $\boldsymbol{j}$ or $\boldsymbol{\tau}$) represents the unknown to be obtained, $\boldsymbol{U}$ the volume average of $\boldsymbol{u}(\boldsymbol{x})$, $\epsilon(\boldsymbol{x})$ the known functions of the local conductivity, $\boldsymbol{A}, \boldsymbol{B}$ are discrete Green operator with an explicit expression in Fourier space (see Table 1).

In section 2, it has been shown that we need to solve equations (8) with a temperature dependent source term. We consider the case where the source term s is a linear function of the local values of $\boldsymbol{e}$ or $\boldsymbol{j}$ or θ, i.e

$$s(\boldsymbol{x}) = \boldsymbol{\alpha}_e(\boldsymbol{x})\boldsymbol{e}(\boldsymbol{x}) + \boldsymbol{\alpha}_j(\boldsymbol{x})\boldsymbol{j}(\boldsymbol{x}) + \alpha_\theta(\boldsymbol{x})\theta(\boldsymbol{x}) + \alpha_0(\boldsymbol{x}) \tag{28}$$

where $\boldsymbol{\alpha}_e(\boldsymbol{x}), \boldsymbol{\alpha}_j(\boldsymbol{x}), \alpha_\theta(\boldsymbol{x})$ and $\alpha_0(\boldsymbol{x})$ are known fields, thus independent from the solution $\boldsymbol{e}$ or $\boldsymbol{j}$ or θ. Since the source term must have zero mean $\langle s(\boldsymbol{x})\rangle = 0$ and $\theta(\boldsymbol{x}) = \Theta + \widetilde{\theta}(\boldsymbol{x})$ from (26), the following relation must be verified

$$-\langle \alpha_\theta(\boldsymbol{x})\rangle \Theta = \langle \boldsymbol{\alpha}_e(\boldsymbol{x})\boldsymbol{e}(\boldsymbol{x}) + \boldsymbol{\alpha}_j(\boldsymbol{x})\boldsymbol{j}(\boldsymbol{x}) + \alpha_\theta(\boldsymbol{x})\widetilde{\theta}(\boldsymbol{x}) + \alpha_0(\boldsymbol{x})\rangle. \tag{29}$$

Name	$\boldsymbol{u}(\boldsymbol{x})$	$\boldsymbol{U}$	$\boldsymbol{A}(\boldsymbol{\xi})$	$\boldsymbol{B}(\boldsymbol{\xi})$	$\epsilon(\boldsymbol{x})$
$\boldsymbol{e}$ scheme	$\boldsymbol{e}(\boldsymbol{x})$	$\boldsymbol{E}$	$\boldsymbol{R}(\boldsymbol{\xi})/\kappa_0$	$-\boldsymbol{P}(\boldsymbol{\xi})$	$\frac{\kappa(\boldsymbol{x})-\kappa_0}{\kappa_0}$
$\boldsymbol{j}$ scheme	$\boldsymbol{j}(\boldsymbol{x})$	$\boldsymbol{J}$	$\boldsymbol{R}(\boldsymbol{\xi})$	$\boldsymbol{Q}(\boldsymbol{\xi})$	$\frac{\kappa(\boldsymbol{x})-\kappa_0}{\kappa(\boldsymbol{x})}$
$\boldsymbol{\tau}$ scheme	$\boldsymbol{\tau}(\boldsymbol{x})$	$\boldsymbol{T}$	$2\boldsymbol{R}(\boldsymbol{\xi})$	$\boldsymbol{H}(\boldsymbol{\xi})$	$\frac{\kappa(\boldsymbol{x})-\kappa_0}{\kappa(\boldsymbol{x})+\kappa_0}$

Table 1: Different iteration schemes with unknown and operators associated to Lippmann-Schwinger equations with source term

The problem (14) can be solved using any one of the four governing equations (22), (23) or (24) and iterate in order to produce the field θ that is consistent with the dynamic equation. Algorithm 1 shows the case of polarization scheme, i.e $\boldsymbol{u} = \boldsymbol{\tau}$ that is used in the paper. The convergence quality of polarization method has been demonstrated in previous publications (see e.g Willot et al., 2014; Moulinec et al., 2018; Monchiet and Bonnet, 2013).

Algorithm 1 Schemes for periodic heat transfer problem with source term

Initialization $\boldsymbol{\tau}^{(0)} = \boldsymbol{T}$

repeat

1. Compute $\boldsymbol{e}^{(n-1)} = \frac{\boldsymbol{\tau}^{(n-1)}}{\kappa(\boldsymbol{x})+\kappa_0}$, $\boldsymbol{j}^{(n-1)} = \frac{\kappa(\boldsymbol{x})\boldsymbol{\tau}^{(n-1)}}{\kappa(\boldsymbol{x})+\kappa_0}$, $\widetilde{\theta}^{(n-1)} = -\mathcal{F}^{-1}\{\boldsymbol{R}^*\mathcal{F}[\boldsymbol{e}^{(n-1)}]\}$
2. Compute $\Theta^{(n-1)}$ from $\boldsymbol{e}^{(n-1)}, \boldsymbol{j}^{(n-1)}$ and $\widetilde{\theta}^{(n-1)}$ by (29) and $\theta^{(n-1)} = \widetilde{\theta}^{(n-1)} + \Theta^{(n-1)}$
3. Compute $s^{(n-1)}$ from $\theta^{(n-1)}$, $\boldsymbol{j}^{(n-1)}$, $\boldsymbol{e}^{(n-1)}$ by (28)
4. Update $\boldsymbol{\tau}^{(n)} = \boldsymbol{T} + \mathcal{F}^{-1}\{2\boldsymbol{R}\mathcal{F}[s^{(n-1)}] + \boldsymbol{H}\mathcal{F}[\frac{\kappa(\boldsymbol{x})-\kappa_0}{\kappa(\boldsymbol{x})+\kappa_0}\boldsymbol{\tau}^{(n-1)}]\}$. Equivalently, $\boldsymbol{\tau}^{(n)} = \boldsymbol{\tau}^{(n-1)} - 2\mathcal{F}^{-1}\{\boldsymbol{P}\mathcal{F}[\boldsymbol{j}^{(n-1)}] - \boldsymbol{R}\mathcal{F}[s^{(n-1)}] + \kappa_0\boldsymbol{Q}\mathcal{F}[\boldsymbol{e}^{(n-1)}]\}$

$n \leftarrow n+1$

until convergence criteria is met

Some remarks on the iterative schemes dealing with periodic problems can be made as follows.

i) In the classical homogenization problem where $s = 0$ and with a finite contrast, the local conductivity being bounded by $\kappa_{\min} < \kappa(\boldsymbol{x}) < \kappa_{\max}$, the best choice of the reference conductivity in this case is $\kappa_0 = \sqrt{\kappa_{\min}\kappa_{\max}}$ for $\boldsymbol{\tau}$

scheme. The polarization $\boldsymbol{\tau}$ scheme has shown to have a faster convergence rate than $\boldsymbol{e}$ and $\boldsymbol{j}$ schemes. Furthermore, combined with the modified Green operators, it does not encounter infinite contrast issues.

ii) In the case where the source term s is prescribed $s = \alpha_0(\boldsymbol{x})$ with the condition $\langle \alpha_0(\boldsymbol{x}) \rangle = 0$, step 3 is unnecessary. The temperature field θ is defined up to a constant Θ and the constant $\Theta^{(n-1)}$ in step 2 can be set unchanged and equal to Θ during the whole process. In the opposite case where s depends on the local temperature θ, the constant $\Theta^{(n-1)}$ in step 2 is then chosen to guarantee $\langle s^{(n-1)} \rangle = 0$ by (29). See also applications to Neumann and Dirichlet boundary conditions in iii) and iv).

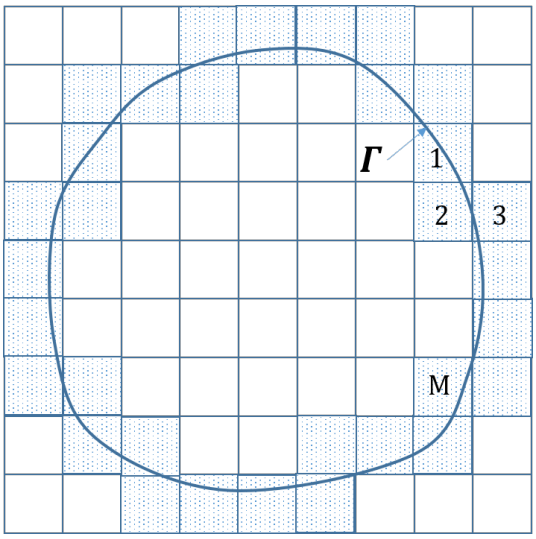

Figure 2: Boundary Γ crossing cells $1, 2, .., M$.

The method can be extended to non periodic problems where the source term can be used to impose heat flux and temperature, for example the immersed interface technique (Peskin, 1972; LeVeque and Li, 1994; Wiegmann). The details of FT implementation using form factor and continuous Green tensors can be found in a recent work (To et al., 2021). Another possibility is to use polarization (or eigenstress/strain for elasticity) as done by Gelebart (2020)

or Chen et al. (2019). For the present problem, the modified Green tensors (Willot et al., 2014) as shown previously and the immersed interface method to deal with perfect or imperfect boundary conditions on pixelized or curved boundary are combined.

iii) Considering the Neumann boundary conditions for normal flux $j_n(\boldsymbol{x})$

$$j_n(\boldsymbol{x}) = j_n^p(\boldsymbol{x}), \quad \boldsymbol{x} \in \Gamma_j \tag{30}$$

on boundary Γ_j which is adjacent to the void phase. Here $j_n^p(\boldsymbol{x})$ is the prescribed normal flux. The void can be considered as a material with zero conductivity. If the Γ_j is approximated to follow the pixel boundary, crossing the cells located at $\boldsymbol{x}_1, \boldsymbol{x}_2, ..., \boldsymbol{x}_M$ (see Fig.2), the normal flux at $\boldsymbol{x}_i$ is related to the source term at $\boldsymbol{x}_i$ by

$$s(\boldsymbol{x}_i)h = j_n^p(\boldsymbol{x}_i) \tag{31}$$

and h is the cell dimensions. In the general case where Γ_j is a known curve boundary curvature significantly different from the previous pixel based boundary, the source term can be evaluated by a more general formula

$$h^3 s(\boldsymbol{x}_i) = \int_{\Gamma_j^i} j_n^p(\boldsymbol{x}) ds \simeq j_n^p(\boldsymbol{x}_i)|\Gamma_j^i| \tag{32}$$

where Γ_j^i is the portion of Γ_j in the cell i.

iv) The Dirichlet type boundary conditions for temperature

$$\theta(\boldsymbol{x}) = \theta^p(\boldsymbol{x}), \quad \boldsymbol{x} \in \Gamma_t \tag{33}$$

are applied to a boundary Γ_t and the source term is known outside Γ_t. In this case, $\theta^p(\boldsymbol{x})$ is the prescribed temperature. The boundary Γ_t is not necessary

adjacent to the void phase as Γ_j of the previous case. Again, the source term s can be used to control the temperature in the cell crossed by Γ_t , for example $\theta(\boldsymbol{x}_i) = \theta_i^p$, $i = 1, 2, .., M$. Such constraint can be imposed by the penalty technique, leading to

$$s^{(n)}(\boldsymbol{x}_i) = \kappa_{pen}(\theta^{(n-1)}(\boldsymbol{x}_i) - \theta_i^p) \tag{34}$$

with large value of κ_{pen}. The other technique is to use the augmented Lagrange technique, coupled with iteration

$$s^{(n)}(\boldsymbol{x}_i) = s^{(n-1)}(\boldsymbol{x}_i) + \kappa_L(\theta^{(n-1)}(\boldsymbol{x}_i) - \theta_i^p) \tag{35}$$

where κ_L is the Lagrange coefficient, usually taken $\kappa_L = \kappa_0$. The integration constant $\Theta^{(n-1)}$ in step 2 can be chosen to ensure the vanishing average source

$$\sum_{\boldsymbol{x}_i \in \Gamma_t} s^{(n)}(\boldsymbol{x}_i) + \sum_{\boldsymbol{x}_i \notin \Gamma_t} s(\boldsymbol{x}_i) = 0 \tag{36}$$

at each time step n by (29). Specifically, we have for penalty technique

$$\sum_{\boldsymbol{x}_i \in \Gamma_t} \kappa_{pen}(\widetilde{\theta}^{(n-1)}(\boldsymbol{x}_i) + \Theta^{(n-1)} - \theta_i^p) + \sum_{\boldsymbol{x}_i \notin \Gamma_t} s(\boldsymbol{x}_i) = 0 \tag{37}$$

or

$$\Theta^{(n-1)} = \frac{1}{M}\left\{ \sum_{\boldsymbol{x}_i \in \Gamma_t} \kappa_{pen}(\theta_i^p - \widetilde{\theta}^{(n-1)}(\boldsymbol{x}_i)) - \sum_{\boldsymbol{x}_i \notin \Gamma_t} s(\boldsymbol{x}_i) \right\} \tag{38}$$

and for augmented Lagrange technique

$$\sum_{\boldsymbol{x}_i \in \Gamma_t} s^{(n-1)}(\boldsymbol{x}_i) + \kappa_L(\Theta^{(n-1)} + \widetilde{\theta}^{(n-1)}(\boldsymbol{x}_i) - \theta_i^p) + \sum_{\boldsymbol{x}_i \notin \Gamma_t} s(\boldsymbol{x}_i) = 0 \tag{39}$$

or

$$\Theta^{(n-1)} = \frac{1}{M}\left\{\kappa_L(\theta_i^p - \widetilde{\theta}^{(n-1)}(\boldsymbol{x}_i)) - \sum_{\boldsymbol{x}_i \notin \Gamma_t} s(\boldsymbol{x}_i) - \sum_{\boldsymbol{x}_i \in \Gamma_t} s^{(n-1)}(\boldsymbol{x}_i)\right\}. \tag{40}$$

v) The temperature jump condition on the boundary Γ_{int} adjacent to the void. The normal flux on Γ_{int} is proportional to the temperature difference and κ_{int} is the interface coefficient

$$j_n(\boldsymbol{x}) = \kappa_{int}(\theta(\boldsymbol{x}) - \theta^p(\boldsymbol{x})), \quad \boldsymbol{x} \in \Gamma_{int}. \tag{41}$$

In this case, the heat exchange at $\boldsymbol{x}_1, \boldsymbol{x}_2, ..., \boldsymbol{x}_M$ where the material is in contact with the temperature θ_i^p, $i = 1, 2, .., M$ is given by

$$hs^{(n)}(\boldsymbol{x}_i) = \kappa_{int}(\theta^{(n-1)}(\boldsymbol{x}_i) - \theta_i^p) \tag{42}$$

for a pixel based boundary and by

$$h^3 s^{(n)}(\boldsymbol{x}_i) = \kappa_{int}(\theta^{(n-1)}(\boldsymbol{x}_i) - \theta_i^p)|\Gamma_{int}^i| \tag{43}$$

for a curved boundary.

vi) The standard convergence criteria of the algorithm is based on the integrability of $\boldsymbol{e}$

$$\varepsilon_e = \|i\boldsymbol{k}(\boldsymbol{\xi}) \times \widehat{\boldsymbol{e}}^{(n)}(\boldsymbol{\xi})\|_F < \overline{\varepsilon}_e \tag{44}$$

and the conservation of energy associated to $\boldsymbol{j}$

$$\varepsilon_j = \|i\boldsymbol{k}^*(\boldsymbol{\xi})\widehat{\boldsymbol{j}}^{(n)}(\boldsymbol{\xi}) + \widehat{s}^{(n)}(\boldsymbol{\xi})\|_F < \overline{\varepsilon}_j \tag{45}$$

which results in the combined criteria

$$\varepsilon_{je} = \max\{\varepsilon_e, \varepsilon_j\} < \overline{\varepsilon}_{je} = \min\{\overline{\varepsilon}_e, \overline{\varepsilon}_j\} \tag{46}$$

where $\varepsilon_e, \varepsilon_j, \varepsilon_{je}$ are error norms and $\overline{\varepsilon}_e, \overline{\varepsilon}_j, \overline{\varepsilon}_{je} \ll 1$ are the smallness parameter controlling the accuracy of the solution. In the case where there are temperature constraints at $\boldsymbol{x}_1, \boldsymbol{x}_2, ..., \boldsymbol{x}_M$, an additional error tolerance ε_θ on temperature is adopted

$$\varepsilon_\theta = \max_{i=1..M} |\theta^{(n)}(\boldsymbol{x}_i) - \theta_i^p| < \overline{\varepsilon}_\theta. \tag{47}$$

The global error and global tolerance are denoted as

$$\varepsilon = \max\{\varepsilon_{je}, \varepsilon_\theta\} < \overline{\varepsilon}. \tag{48}$$

The frequency dependent heat transfer problem is the particular case of the general problem considered in the previous section.Two phases are present: the gas (conductivity κ_g) and the solid (conductivity κ_s). The temperature to solve is called the excess temperature θ which is considered as being null ($\theta(\boldsymbol{x}) = 0$) in the solid phase. Due to the similar nature of the two equations (7) and (2), the acoustic wave problem (2) in gas filled porous material will be dealt as an example.

In this case, the average flux, gradient and polarization do not exist $\boldsymbol{E} = \boldsymbol{J} = \boldsymbol{T} = 0$ and the internal field is induced by the source term s which is known in the gas phase

$$s = -i\omega P + i\omega\rho_g c_g \theta \quad \text{in the gas phase} \tag{49}$$

and unknown in the solid phase.

The two types of boundary conditions can be treated by Algorithm 1. For

ideal boundary conditions, the augmented lagrangian with temperature constraints is applied to either the boundary cell or the whole solid phase. In this case, the value of the conductivity κ_s does not affect the solution of our problem but its choice can have impacts on the convergence behavior. The numerical experiments show that setting $\kappa_s = 100 - 1000\kappa_g$ and global tolerance $\overline{\varepsilon} = 0.001 - 0.0001$ will yield the optimal value between computation cost and accuracy. Regarding imperfect boundary conditions, we set $\kappa_s = 0$ so that the normal flux is equal to the source term as before. Additionally, since the resulting flux is proportional to the measure of the boundary and thus affects the source term s, results can be sensitive to the choice of pixel based or curved boundary.

4. Generalized scheme based on frequency dependent Green operators

Up to now, the Green operators $\boldsymbol{P}, \boldsymbol{Q}, \boldsymbol{H}$ and $\boldsymbol{R}$ are obtained for a homogeneous media of conductivity κ_0 and the heterogeneity effect of conductivity is accounted for by the polarization. For systems involving variation of internal heat energy, the source term s can be further decomposed into a heat generation $\tilde{s}$ and a source term coming from the thermal capacity as

$$s = \tilde{s} + i\omega\rho c\theta \tag{50}$$

where ρc is the heat capacity. Then, the Green operators can be generalized to account for the heat capacity of the reference media $\rho_0 c_0$. It is noted that a similar treatment is used in the context of homogenization of Bloch wave in elastodynamics (see e.g Srivastava and Nemat-Nasser, 2012, and the references therein) For the present heat transfer problem, let us pose

$$s' = \tilde{s} + i\omega(\rho c - \rho_0 c_0)\theta = s - i\omega\rho_0 c_0\theta \tag{51}$$

This shows that the use of the reference capacity introduces a new polarization term $i\omega(\rho c - \rho_0 c_0)\theta$. Inserting this relation into (22) in Fourier space and noting that $\widehat{\theta}(\boldsymbol{\xi}) = -\boldsymbol{R}^*(\boldsymbol{\xi})\widehat{\boldsymbol{e}}(\boldsymbol{\xi})$ from (26) and $\boldsymbol{R}(\boldsymbol{\xi})\boldsymbol{R}^*(\boldsymbol{\xi}) = 1/|\boldsymbol{k}|^2$ via (20), we obtain

$$\left[1 + \frac{i\omega\rho_0 c_0}{\kappa_0|\boldsymbol{k}|^2}\right]\widehat{\boldsymbol{e}}(\boldsymbol{\xi}) = \frac{1}{\kappa_0}\boldsymbol{R}(\boldsymbol{\xi})\widehat{s'}(\boldsymbol{\xi}) - \frac{1}{\kappa_0}\boldsymbol{P}(\boldsymbol{\xi})\widehat{(\kappa - \kappa_0)\boldsymbol{e}}(\boldsymbol{\xi}), \quad \forall \boldsymbol{\xi} \neq 0. \tag{52}$$

Passing the term $\left[1 + \frac{i\omega\rho_0 c_0}{\kappa_0|\boldsymbol{k}|^2}\right]$ to the right side of the equation and returning to the real space yields

$$\boldsymbol{e}(\boldsymbol{x}) = \boldsymbol{E} + \frac{1}{\kappa_0}\boldsymbol{R}' * s' - \frac{1}{\kappa_0}\boldsymbol{P}' * (\kappa - \kappa_0)\boldsymbol{e}, \tag{53}$$

with the new Green tensors $\boldsymbol{R}', \boldsymbol{P}'$

$$\boldsymbol{R}'(\boldsymbol{\xi}) = \frac{i\boldsymbol{k}}{|\boldsymbol{k}|^2 + \frac{i\omega\rho_0 c_0}{\kappa_0}}, \quad \boldsymbol{P}'(\boldsymbol{\xi}) = \frac{\boldsymbol{k} \otimes \boldsymbol{k}^*}{|\boldsymbol{k}|^2 + \frac{i\omega\rho_0 c_0}{\kappa_0}}, \quad \forall \boldsymbol{\xi} \neq 0. \tag{54}$$

Similar expressions can be derived for flux $\boldsymbol{j}$ and polarization $\boldsymbol{\tau}$

$$\boldsymbol{j}(\boldsymbol{x}) = \boldsymbol{J} + \boldsymbol{R}' * s' + \boldsymbol{Q}' * \frac{\kappa - \kappa_0}{\kappa}\boldsymbol{j}, \tag{55}$$

and

$$\boldsymbol{\tau}(\boldsymbol{x}) = \boldsymbol{T} + 2\boldsymbol{R}' * s' + \boldsymbol{H}' * \frac{\kappa - \kappa_0}{\kappa + \kappa_0}\boldsymbol{\tau}, \tag{56}$$

with $\boldsymbol{Q}', \boldsymbol{H}'$ defined as

$$\boldsymbol{Q}'(\boldsymbol{\xi}) = \boldsymbol{I} - \boldsymbol{P}'(\boldsymbol{\xi}), \quad \boldsymbol{H}'(\boldsymbol{\xi}) = \boldsymbol{Q}'(\boldsymbol{\xi}) - \boldsymbol{P}'(\boldsymbol{\xi}), \quad \forall \boldsymbol{\xi} \neq 0 \tag{57}$$

Like $\boldsymbol{R}, \boldsymbol{P}, \boldsymbol{Q}, \boldsymbol{H}$, the tensors $\boldsymbol{R}', \boldsymbol{P}', \boldsymbol{Q}', \boldsymbol{H}'$ vanish at $\boldsymbol{\xi} = \boldsymbol{0}$, or $\boldsymbol{P}'(\boldsymbol{0}) = \boldsymbol{Q}'(\boldsymbol{0}) = \boldsymbol{H}'(\boldsymbol{0}) = 0$. It is noted that if the composite ratio $\omega\rho_0 c_0/\kappa_0 \to 0$,

we recover the original expressions $\boldsymbol{R}' = \boldsymbol{R}$, $\boldsymbol{P}' = \boldsymbol{P}$, $\boldsymbol{Q}' = \boldsymbol{Q}$, $\boldsymbol{H}' = \boldsymbol{H}$.

We find that LS equations (53), (55) and (56) based on the frequency and heat capacity dependent Green operators $\boldsymbol{P}', \boldsymbol{Q}'$ and $\boldsymbol{H}'$ have the same structure as (22), (23) and (24). As a result, the iteration method can be based on Algorithm 1 with suitable modification. The modified source term s' becomes

$$s' = -i\omega P + i\omega(\rho c - \rho_0 c_0)\theta \quad \text{in the gas phase} \tag{58}$$

and is unknown in the solid phase. To enforce the given temperature at the solid phase, the penalty and the augmented Lagrange techniques are applied to s like in the original scheme to ensure (36) and s' is calculated by the formula

$$s'^{(n)} = s^{(n)} - i\omega\rho_0 c_0 \theta^{(n-1)}. \tag{59}$$

As a result when $\rho_0 c_0 = 0$, the scheme associated to the frequency dependent tensor is exactly the same as in the original scheme.

5. Numerical applications

In the previous sections, two kinds of Green tensors, the static and dynamic ones were presented. Since the first one leads to converging results, the results are presented in the first two subsections by using the static Green tensor . Next, the dynamic Green tensor is introduced in the last subsection in order to evaluate the capacity of the related numerical scheme, compared to the one related to static Green tensor.

5.1. Heat transfer with an ideal boundary

The two 2D problems where analytical solution is available (see Appendix) will be considered first. The unit cell has dimensions $L_1 = L_2 = 1$ and the resolution parameter is fixed at $N = 128$, or resolution 256×256

in real space. Other parameters of the simulation are: $\kappa_g = 1$, $\kappa_s = 100$, $\kappa_0 = \sqrt{\kappa_g \kappa_s} = 10$ and global tolerance $\overline{\varepsilon} = 0.001$. The ideal boundary condition is applied at the solid gas interface and the augmented Lagrange technique is used to control the temperature of the solid phase. The iteration scheme based on the original Green tensors will be used. The program is written using Matlab and all the simulations are run on a laptop computer under Windows 10 OS with Intel Core i5-10310U CPU 1.70GHz RAM 16 GB.

In the first problem, the gas is inside a parallel slit pore of width $2a = 2/3$ and the characteristic length is fixed $\kappa_g/\omega\rho_g c_g = 1$ (or $\delta = 1/\sqrt{i}$). After 39 iterations which takes 1.00 s, the algorithm converges, yielding results given in Fig 3. From the real temperature field, it is zero outside the gas phase and increases around the center due to the effect of the source term. The temperature profile cutting across the unit cell confirms this trend and shows that both the real and imaginary parts of the temperature match perfectly the analytical solutions given in the Appendix.

In the second problem, the gas is contained inside the cylindrical pore with radius $a = 1/3$. The characteristic length parameters are varied $\kappa_g/\omega\rho_g c_g = 1$, 0.02, 0.01. The algorithm stops after 45, 78, 104 iterations (or 1.02s, 1.65s, 2.20s computation time) and results are plotted in Fig. 4. Again, the temperature is zero in the solid phase and the solution in the gaseous phase agrees with the analytical solutions. It is noted that when $\kappa_g/\omega\rho_g c_g$ and δ decreases, the behavior corresponds to a lower diffusivity/conductivity and the temperature profile tends to decrease and flatten out. Theoretically, the temperature field tends to a vanishing small field $\theta \to 0$ when $\delta \to 0$. When δ increases, the conductive behavior becomes increasingly dominant. Numerical evidence shows that when $\kappa_g/\omega\rho_g c_g \geq 1$, the temperature profile is stabilized and less sensitive to the parameter $\kappa_g/\omega\rho_g c_g$.

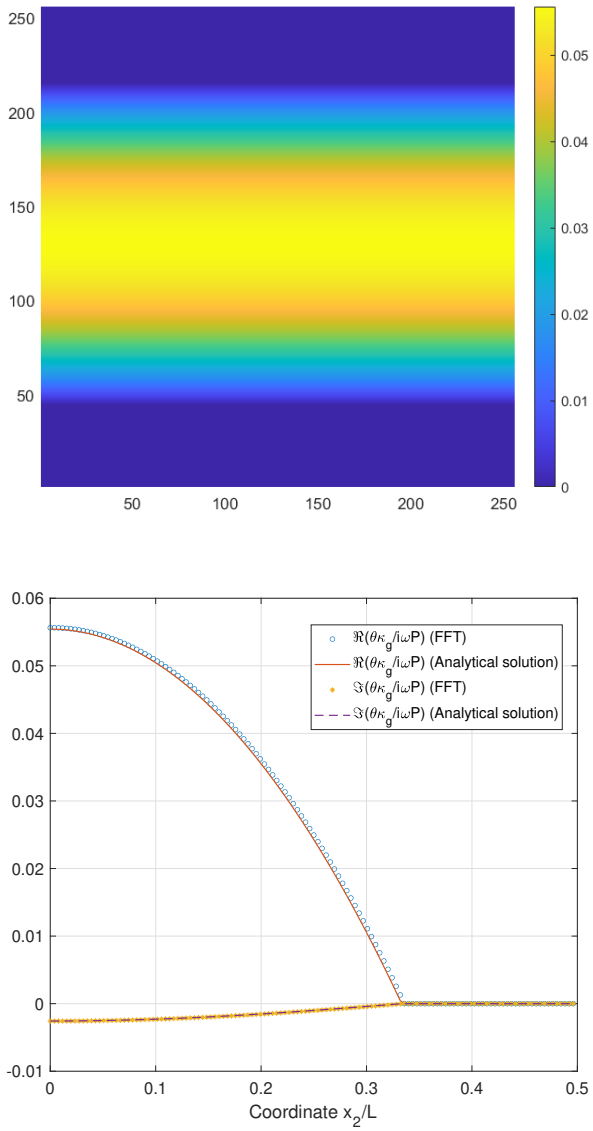

Figure 3: The case of parallel pore with perfect solid-gas interface. The real part of temperature field $\Re(\kappa_g\theta/i\omega P)$ (top) and the variation of the real and imaginary part of temperature along axis x_2 (bottom).

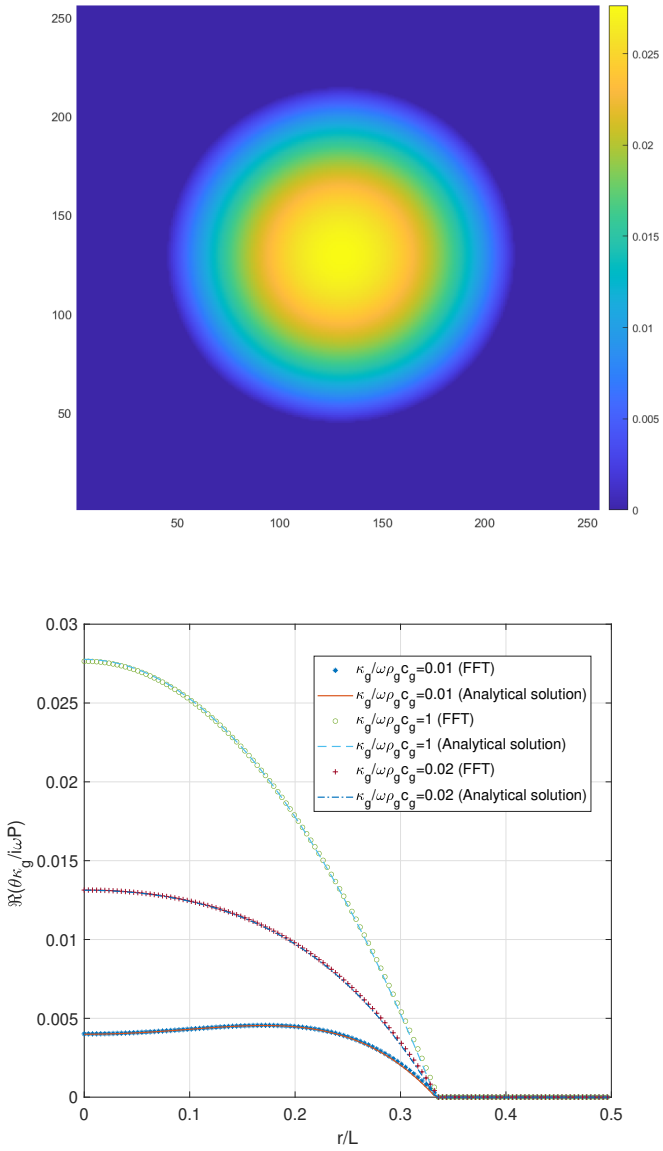

Figure 4: The case of circle pore with perfect solid-gas interface. The real part of temperature field $\Re(\kappa_g\theta/i\omega P)$ with $\kappa_g/\omega\rho_g c_g = 1$ (top) and the variation of the real part of temperature on axis x_2 at different value of $\kappa_g/\omega\rho_g c_g$ (bottom).

Next we shall consider a problem on a fiber material containing a random setting of cylindrical fibers. The sample section containing 15 random non-overlapping circles of radius 0.06 is generated by the Random Sequential Addition (RSA). The cylinder represents the solid phase and the pore corresponds to the space between the cylinders. We are interested by the convergence behavior of the problem, i.e the variation of errors ε_{je} and ε_θ with respect to the number of iterations. From Fig. 5, the error norms exhibit a common two regimes behavior: a steep descent followed by a slower descent. This two regimes behaviour is also found in the recent work on the convergence of FFT based iterative schemes (Moulinec et al., 2018). It is noted that our error norm exhibits some curvature rather than straight lines in (Moulinec et al., 2018). It is suggested that implementation of temperature constraints has some effects on the variation trend of the error norm. While the slope of the slow descent is relatively similar for all error norms, the slope and the extent of the steep descent depend on κ_s. Using high values of κ_s accelerates the convergence and leads to a small error value earlier and before starting the slow regime.

5.2. Thermal permeability problem with temperature jump boundary

In this subsection, the performance of the algorithm for imperfect boundary condition will be studied. Let us study again the first two examples, parallel pore and circle pore with the same parameters as in the previous section and introduce the interface coefficient $l = \delta = 1/\sqrt{i}$ (or $\kappa_{int} = \kappa_g/\delta$) at the solid gas boundary. The global tolerance is the same as the previous case $\overline{\varepsilon} = 0.001$. We note that for normal homogenization problems of heterogeneous materials, to achieve the best convergence rate, the reference conductivity κ_0 should be taken as $\kappa_0 = \sqrt{\kappa_{\min}\kappa_{\max}}$ and the two positive values $\kappa_{\max}, \kappa_{\min}$ are the upper and lower bounds of the local conductivity. Under the special problem with presence of the interfaces, the void phase and the external source at the interface, the optimal reference conductivity κ_0, is generally unknown and must be studied case by case.

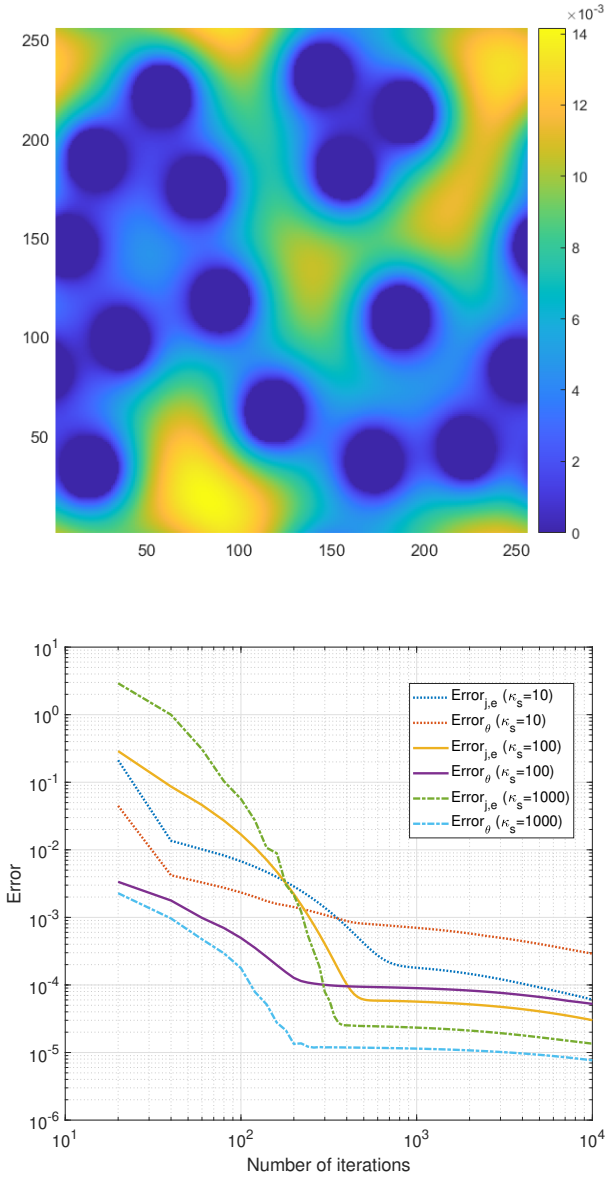

Figure 5: The case of fiber material with perfect solid-gas interface. The radius of the fibers is 0.06 and the porosity is $\nu = 0.8221$. The real part of temperature field $\Re(\kappa_g\theta/i\omega P)$ (top) and the variation error norms with respect to the number of iteration (bottom).

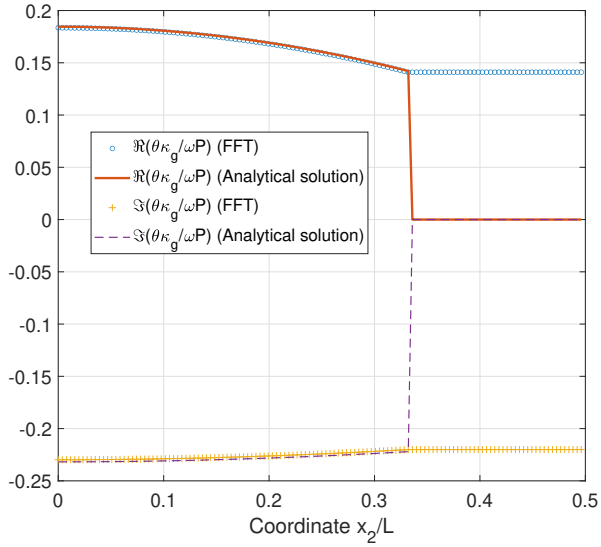

Figure 6: The case of parallel pore with temperature jump at solid-gas interface. The variation of the real and imaginary part of temperature on axis x_2 for.

In the slit pore problems, it is found that the FFT method has a good performance. Specifically, with $\kappa_0 = \kappa_g$, we need 4 iterations (0.15 s) to reach the global accuracy $\overline{\varepsilon}$ and the results compare well with the analytical solution. Both imaginary and real parts produce the jump value at the interface and the variation in the pore is also the same (see Fig. 6). In the figure, the temperature in the solid phase obtained by FFT method is not zero because we are interested only in the gas temperature. The solid conductivity is set to zero ($\kappa_s = 0$) and the heat exchange between the solid and the gas is accounted for by the source term. It is noted that for slit pore, the real interface nearly coincides with the pixel based boundary at the resolution $N = 128$.

For the cylindrical pore problem (see Fig. 7), we observe a significant difference between the scheme without curve correction (42) and the one using pixel based approximation (43). So, the comparison ls made also with curve

correction in the source term. Without the correction, the resulting source term which is proportional to the measure of the boundary can be over or underevaluated. This results in a deviation from the analytical solution. When taking account for the length of the circle crossing the cell, the agreement is excellent. The convergence is also fast as with $\kappa_0 = \kappa_g$, the algorithm stops after 15 iterations (or 0.35 s)

It can be concluded that to study interface effects, the evaluation of the boundary flux is important and requires an accurate description of the boundary length in the cells.
Next the problem of fiber material with varying slip length l from $10^{-3}\delta$ to $10^{5}\delta$ is considered. To ensure the convergence, the reference conductivity κ_0 must also vary, especially for small values of slip length l, near an ideal interface regime. It requires an increasing value of κ_0 in these cases and the convergence is slower. For example, for $l = 0.001\delta$, we need $\kappa_0 = 1000\kappa_g$ and 11707 iterations (or 250 s). For moderate and high slip $l \geq 0.1\delta$, the method based on penalty technique is very fast, with a number of iterations ranging from 10 to 200. Looking at the temperature field in Fig. 8, a significant effect of the slip length on the solution can be observed. When the slip length increases, there is no resistance at the interface and the solid phase tends to facilitate the heat flow in the gas. Consequently, the temperature field in the gas is much more homogeneous.
At the limit case, the homogeneous temperature field is expected to satisfy (2) and the temperature field can be obtained

$$\theta = -\frac{i\omega P}{\kappa_g}\delta^2 \tag{60}$$

and the thermal permeability $\overline{\Theta}$ according to (9)

$$\overline{\Theta}(\delta(\omega)) = -\delta^2. \tag{61}$$

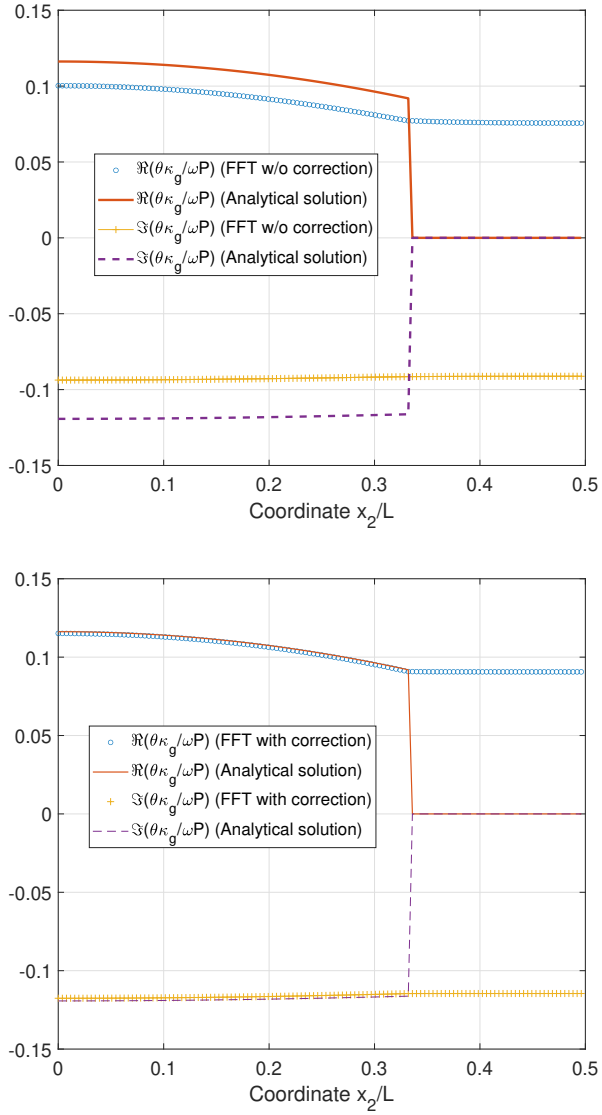

Figure 7: The case of circle pore with temperature jump at solid-gas interface. The variation of the real and imaginary part of temperature on axis x_2 using two formulations: without curve correction (42) (top) and with curve correction (43) (bottom).

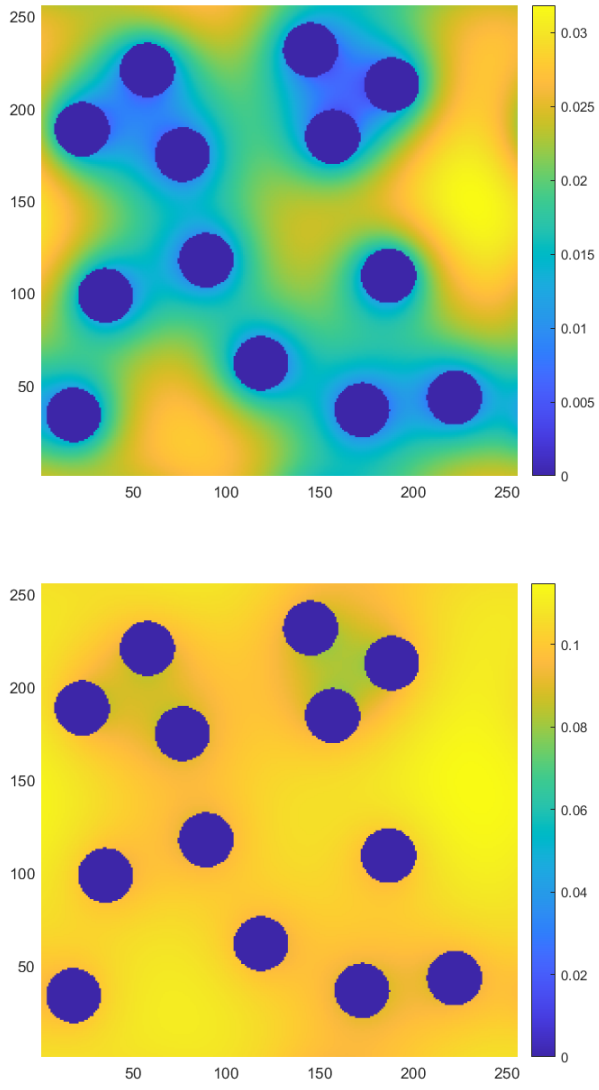

Figure 8: The case of fiber material with temperature jump at solid-gas interface. The radius of the fibers is 0.06 and the porosity is $\nu = 0.865$. The real part of temperature field $\Re(\kappa_g \theta / i\omega P)$ at $l = 0.1\delta$ (top) and $l = \delta$ (bottom).

With $\delta = 1/\sqrt{i}$, these theoretical limits agree with the numerical results in Fig. 9 as we found $\Re[\overline{\Theta}] = 0$ and $\Im[\overline{\Theta}] = -1$ at high value of thermal slip. It is interesting to remark the different behavior of $\Re[\overline{\Theta}]$ and $\Im[\overline{\Theta}]$: $\Re[\overline{\Theta}]$ first increases to a peak, around $l/\delta = 5$ before decreasing to 0 and $\Im[\overline{\Theta}]$ monotonically decreases to -1.

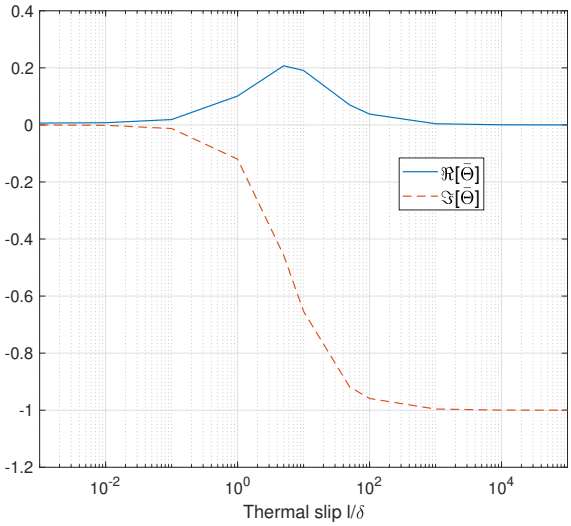

Figure 9: The real and imaginary part of effective thermal permeability $\overline{\Theta}$ as function of thermal slip length l/δ. The complex length is fixed at $\delta = 1/\sqrt{i}$.

5.3. Comparison of the results obtained using static or frequency dependent tensor schemes

Up to now , all results have been obtained by using the "static" Green tensor. So, in this subsection, the comparison is made between the results obtained from both Green tensors. A firt result is that the frequency dependent tensor schemes $\boldsymbol{P'}, \boldsymbol{Q'}, \boldsymbol{R'}, \boldsymbol{H'}$ yield the same solution at convergence as the original scheme for all the problems considered in the previous subsection. In terms of convergence rates, they are obviously the same when the reference heat capacity vanishes $\rho_0 c_0 = 0$. To achieve the comparison, the new scheme is used by varying the reference parameter $\rho_0 c_0$, which can be an

$\frac{\rho_0 c_0}{\rho_g c_g}$	N_{iter}	$\frac{\rho_0 c_0}{\rho_g c_g}$	N_{iter}	$\frac{\rho_0 c_0}{\rho_g c_g}$	N_{iter}
-0.6	very slow	$-10^3 i$	97	$-0.7e^{i\pi/4}$	341
-0.5	456	$-10^2 i$	48	$-0.6e^{i\pi/4}$	49
-0.1	45	$-10i$	45	$-0.1e^{i\pi/4}$	45
-0.01	45	$-i$	45	$-0.01e^{i\pi/4}$	45
0	45	-	-	-	-
0.01	45	i	45	$0.01e^{i\pi/4}$	45
0.1	45	$10i$	51	$0.1e^{i\pi/4}$	45
0.5	441	$10^2 i$	diverge	$0.6e^{i\pi/4}$	49
0.6	very slow	$10^3 i$	diverge	$0.7e^{i\pi/4}$	338

Table 2: Number of iterations at convergence as a function of reference heat capacity $\rho_0 c_0$ for cylindrical pore problem. As for computation time, it varies from 1.10 s for 45 iterations to 7.40s for 338 iterations.

arbitrary complex number. Let us pose $\rho_0 c_0/\rho_g c_g = re^{i\varphi}$ with r being a real number and $\varphi = 0, \pi/4, \pi/2$. The problems of slit pore and cylindrical pore with perfect boundary conditions and parameters $\kappa_s = 100$, $\kappa_g/\omega\rho_g c_g = 1$ are considered as examples.

From Table 2 for cylindrical pore problem, it is found that the convergence is sensitive to the reference parameter. For all cases under consideration, the best convergence is achieved when $\rho_0 c_0 = 0$ or $|\frac{\rho_0 c_0}{\rho_g c_g}|$ is small. When $\frac{\rho_0 c_0}{\rho_g c_g}$ reaches a certain threshold value, the error norm decreases very slowly or even increases (divergence). The convergence behavior is symmetric if $\frac{\rho_0 c_0}{\rho_g c_g}$ is real or in the form $\frac{\rho_0 c_0}{\rho_g c_g} = re^{i\pi/4}$. The number of iterations remains relatively low and then changes drastically at $|\frac{\rho_0 c_0}{\rho_g c_g}| = 0.6 - 0.7$. The behavior is different when $\frac{\rho_0 c_0}{\rho_g c_g}$ is purely imaginary. The scheme still converges well at much higher value $|\frac{\rho_0 c_0}{\rho_g c_g}|$ and diverges when $\frac{\rho_0 c_0}{\rho_g c_g} = 100i$. It is suggested that this behavior can be linked to the singularity of the new Green tensors. It is noted that the term $i\omega\rho_0 c_0/\kappa_0$ can be negative and the denominator $|\boldsymbol{k}|^2 + i\omega\rho_0 c_0/\kappa_0$ of the new Green tensors can be singular for some values of $\boldsymbol{k}$.

$\frac{\rho_0 c_0}{\rho_g c_g}$	N_{iter}	$\frac{\rho_0 c_0}{\rho_g c_g}$	N_{iter}	$\frac{\rho_0 c_0}{\rho_g c_g}$	N_{iter}
-1000	286	$-10^3 i$	127	$-1000e^{i\pi/4}$	145
-100	44	$-10^2 i$	53	$-100e^{i\pi/4}$	51
-10	45	$-10i$	45	$-10e^{i\pi/4}$	45
-1	39	$-i$	41	$-e^{i\pi/4}$	39
0	39	-	-	-	-
1	41	i	39	$e^{i\pi/4}$	39
10	45	$10i$	47	$10e^{i\pi/4}$	47
100	46	$10^2 i$	diverge	$100e^{i\pi/4}$	118
1000	230	$10^3 i$	diverge	$1000e^{i\pi/4}$	diverge

Table 3: Number of iteration at convergence as a function of reference heat capacity $\rho_0 c_0$ for slit pore problem. As for computation time, it varies from 1.0 s for 39 iterations to 2.50s for 118 iterations.

For the problem of slit pore (see Table 3), a behavior similar to the one of cylindrical pore is observed. There is some small difference in the fact that the scheme is stable for a larger range of $\frac{\rho_0 c_0}{\rho_g c_g}$, especially when $\frac{\rho_0 c_0}{\rho_g c_g}$ is real or not purely imaginary. The scheme converges relatively well up to $|\frac{\rho_0 c_0}{\rho_g c_g}| = 100 - 1000$, compared to $|\frac{\rho_0 c_0}{\rho_g c_g}| = 0.6 - 0.7$ for the cylindrical pore. This is a special problem where the heat transfer is along one direction only. It suggests that the particularity of the solution renders the spectral property of the scheme less sensitive to $\rho_0 c_0$. From these two examples, we find that the dynamic Green tensor, though being a priori more "adapted" to the dynamic equation, does not improve in any way the speed or convergence, compared to the static Green tensor. The best convergence being observed when the heat capacity is set to zero in the dynamic Green tensor.

6. Concluding remarks

In the present paper, the Fourier Transform method is developed to solve the frequency dependent heat transfer problem. The main ingredient of the method is the LS equation for heat transfer problem based on discrete Green operators. The source term appearing in the equation is used to capture

the harmonic fluctuation of pressure and to enforce the constraints at the boundary. Both ideal and temperature jump boundary conditions can also be modelled by the method. From the applications to different microstructures, the method proves to be fast and to yield accurate results.

A generalized scheme based on a dynamic Green tensors is also proposed. Analogous to elastodynamics, those frequency dependent tensors are derived by using a reference complex heat capacity $\rho_0 c_0$. While being more flexible, the scheme converges equally well at small value of $\rho_0 c_0$. Equivalently, the optimal convergence of the generalized scheme is recovered in the particular case where the dynamic Green tensor coincides with the static Green tensor.

The use of source terms was shown in a previous work to be very useful when solving boundary value problems using FFT formulation (To et al., 2021). This work shows that the introduction of these source terms can be also of interest when the sources are frequency-dependent as in the case of dynamic heat conduction.

Appendix A. Analytical solutions for 2D heat transfer problems with temperature jump

For parallel pore of width $2a$ limited by the inequality $-a < x_2 < a$ (see Fig. A10a), the solution $\theta(x_2)$ in the gas phase must satisfy

$$\theta''(x_2) - \frac{\theta(x_2)}{\delta^2} + \frac{i\omega P}{\kappa_g} = 0. \tag{A.1}$$

The general solution

$$\theta = \frac{P}{\rho_g c_g} + Ae^{x_2/\delta} + Be^{-x_2/\delta} \tag{A.2}$$

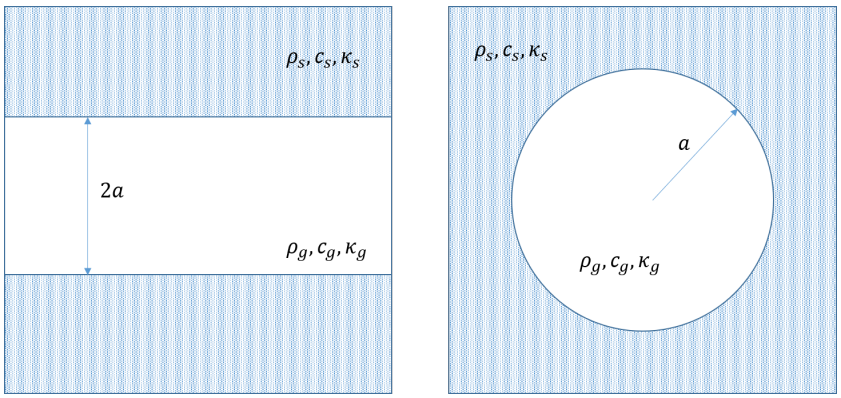

Figure A.10: Microstructures of two examples.

combined with the boundary conditions at the gas-solid interface

$$\theta(a) = -l\theta'(a), \quad \theta(-a) = l\theta'(-a) \tag{A.3}$$

yield the analytical solution

$$\theta = \frac{P}{\rho_g c_g}\left[1 - \frac{e^{x_2/\delta} + e^{-x_2/\delta}}{(e^{a/\delta} + e^{-a/\delta}) + l/\delta(e^{a/\delta} - e^{-a/\delta})}\right]. \tag{A.4}$$

In the case of perfect interface $l/\delta = 0$, the classical solution is recovered

$$\theta(x_2) = \frac{P}{\rho_g c_g}\left[1 - \frac{e^{x_2/\delta} + e^{-x_2/\delta}}{e^{a/\delta} + e^{-a/\delta}}\right] \tag{A.5}$$

where temperature equal to 0 at $x_2 = \pm a$.

For circular pore of radius a (see Fig. A10b), the governing solution in the cylindrical coordinate for $\theta(r)$ in the gas phase becomes

$$\theta''(r) + \frac{\theta'(r)}{r} - \frac{\theta(r)}{\delta^2} + \frac{i\omega P}{\kappa_g} = 0 \tag{A.6}$$

The general solution has the form

$$\theta(r) = \frac{P}{\rho_g c_g} + AI_0(r/\delta) \tag{A.7}$$

where I_k is the modified Bessel function of first kind and of kth order. Under the boundary conditions at the gas-solid interface is given by

$$\theta(a) = -l\theta'(a) \tag{A.8}$$

The exact solution of the above problem is

$$\theta(r) = \frac{P}{\rho_g c_g}\left[1 - \frac{I_0(r/\delta)}{I_0(a/\delta) + l/\delta I_1(a/\delta)}\right]. \tag{A.9}$$

In the case of perfect interface $l/\delta = 0$, the classical solution is recovered

$$\theta(r) = \frac{P}{\rho_g c_g}\left[1 - \frac{I_0(r/\delta)}{I_0(a/\delta)}\right] \tag{A.10}$$

where temperature equal to 0 at $r = a$.

References

Auriault, J., 1983. Effective macroscopic description for heat conduction in periodic composites. Int. J. Heat Mass Transf. 26, 861–869.

Auriault, J.L., Boutin, C., Geindreau, C., 2010. Homogenization of coupled phenomena in heterogenous media. volume 149. John Wiley & Sons.

Bensoussan, A., Lions, J., Papanicolaou, G., 1978. Asymptotic analysis for periodic structures. North-Holland.

Bignonnet, F., 2020. Efficient FFT-based upscaling of the permeability of

porous media discretized on uniform grids with estimation of RVE size. Comput. Methods Appl. Mech. Eng. 369, 113237.

Boutin, C., Royer, P., Auriault, J., 1998. Acoustic absorption of porous surfacing with dual porosity. Int. J. Solids Structures 35, 4709–4737.

Brisard, S., Dormieux, L., 2010. FFT-based methods for the mechanics of composites: A general variational framework. Comput. Mater. Sci. 49, 663–671.

Brisard, S., Dormieux, L., 2012. Combining Galerkin approximation techniques with the principle of Hashin and Shtrikman to derive a new FFT-based numerical method for the homogenization of composites. Comput. Meth. Appl. Mech. Eng. 217, 197–212.

Brown Jr, W.F., 1955. Solid mixture permittivities. J. Chem. Phys. 23, 1514–1517.

Chastanet, J., Royer, P., Auriault, J.L., 2004. Acoustics with wall-slip flow of gas-saturated porous media. Mech. Res. Commun. 31, 277–286.

Chen, Y., Gelebart, L., Chateau, C., Bornert, M., Sauder, C., King, A., 2019. Analysis of the damage initiation in a SiC/SiC composite tube from a direct comparison between large-scale numerical simulation and synchrotron x-ray micro-computed tomography. Int. J. Solids Struct. 161, 111–126.

De Geus, T., Vondřejc, J., Zeman, J., Peerlings, R., Geers, M., 2017. Finite strain FFT-based non-linear solvers made simple. Comput. Meth. Appl. Mech. Eng. 318, 412–430.

Eyre, D.J., Milton, G.W., 1999. A fast numerical scheme for computing the response of composites using grid refinement. Eur. Phys. J. Appl. Phys. 6, 41–47.

Gelebart, L., 2020. A modified FFT-based solver for the mechanical simulation of heterogeneous materials with Dirichlet boundary conditions. CR Mecanique 348, 693–704.

Kapitza, S.B., 1941. The study of heat transfert in helium II. J. Phys. (USSR) , 181.

Kröner, E., 1977. Bounds for effective elastic moduli of disordered materials. J. Mech. Phys. Solids 25, 137–155.

Lafarge, D., Lemarinier, P., Allard, J.F., Tarnow, V., 1997. Dynamic compressibility of air in porous structures at audible frequencies. J. Acoust. Soc. Am. 102, 1995–2006.

LeVeque, R.J., Li, Z., 1994. The immersed interface method for elliptic equations with discontinuous coefficients and singular sources. SIAM J. Numer. Anal. 31, 1019–1044.

Liao, M., To, Q.D., Léonard, C., Monchiet, V., 2018a. Non-parametric wall model and methods of identifying boundary conditions for moments in gas flow equations. Phys. Fluids 30, 032008.

Liao, M., To, Q.D., Léonard, C., Yang, W., 2018b. Prediction of thermal conductance and friction coefficients at a solid-gas interface from statistical learning of collisions. Phys. Rev. E 98, 042104.

Michel, J., Moulinec, H., Suquet, P., 1999. Effective properties of composite materials with periodic microstructure: a computational approach. Comput. Method Appl. Mech. Eng. 172, 109–143.

Michel, J., Moulinec, H., Suquet, P., 2001. A computational scheme for linear and non-linear composites with arbitrary phase contrast. Int. J. Numer. Meth. Eng. 52, 139–160.

Milton, G.W., 2002. The theory of composites. volume 6. Cambridge University Press.

Monchiet, V., 2018. FFT based iterative schemes for composites conductors with non-overlapping fibers and Kapitza interface resistance. Int. J. Solids Struct. 135, 14–25.

Monchiet, V., Bonnet, G., 2013. A polarization-based fast numerical method for computing the effective conductivity of composites. Int. J. of Num. Meth. for Heat and Fluid Flow 23, 1256–1271.

Moulinec, H., Silva, F., 2014. Comparison of three accelerated FFT-based schemes for computing the mechanical response of composite materials. Int. J. Numer. Meth. Eng. 97, 960–985.

Moulinec, H., Suquet, P., 1994. A fast numerical method for computing the linear and nonlinear mechanical properties of composites. C. R. Acad. Sci 318, 1417–1423.

Moulinec, H., Suquet, P., Milton, G.W., 2018. Convergence of iterative methods based on Neumann series for composite materials: theory and practice. Int. J. Numer.Meth. Eng. 114, 1103–1130.

Nemat-Nasser, S., Hori, M., 2013. Micromechanics: overall properties of heterogeneous materials. volume 37. Elsevier.

Nguyen, T.K., Monchiet, V., Bonnet, G., 2013. A Fourier based numerical method for computing the dynamic permeability of periodic porous media. Eur. J. Mech. B Fluids 37, 90–98.

Peskin, C.S., 1972. Flow patterns around heart valves: a numerical method. J. Comput. Phys. 10, 252–271.

Schneider, M., 2019. On the Barzilai-Borwein basic scheme in FFT-based computational homogenization. Int. J. Numer. Meth. Eng. , 482–494.

Srivastava, A., Nemat-Nasser, S., 2012. Overall dynamic properties of three-dimensional periodic elastic composites. Proc. Math. Phys. Eng. Sci. 468, 269–287.

To, Q.D., Bonnet, G., 2020. FFT based numerical homogenization method for porous conductive materials. Comput. Meth. Appl.Mech. Eng. 368, 113160.

To, Q.D., Bonnet, G., Nguyen, T.T., 2021. Fourier transform approach to non periodic boundary value problems in porous conductive media. Int. J. Numer. Methods Eng. 122, 4864–4885.

Torquato, S., 2001. Random heterogeneous materials: microstructure and macroscopic properties. Springer, Berlin.

Umnova, O., Tsiklauri, D., Venegas, R., 2009. Effect of boundary slip on the acoustical properties of microfibrous materials. J. Acoust. Soc. Am. 126, 1850–1861.

Vondřejc, J., Zeman, J., Marek, I., 2014. An FFT-based Galerkin method for homogenization of periodic media. Comput. Math. with Appl. 68, 156–173.

Wiegmann, A., . Fast Poisson, fast Helmholtz and fast linear elastostatic solvers on rectangular parallelepipeds. Technical Report Lawrence Berkeley National Laboratory .

Willot, F., Abdallah, B., Pellegrini, Y.P., 2014. Fourier-based schemes with modified Green operator for computing the electrical response of heterogeneous media with accurate local fields. Int. J. Numer. Meth. Eng. 98, 518–533.

Zeman, J., Vondrejc, J., Novak, J., Marek, I., 2010. Accelerating a FFT-based solver for numerical homogenization of periodic media by conjugate gradients. J. Comput. Phys , 8065–8071.